

PAPER • OPEN ACCESS

## Laser patterning of large-scale perovskite single-crystal-based arrays for single-mode laser displays



To cite this article: Wangqi Mao *et al* 2023 *Int. J. Extrem. Manuf.* **5** 045001

View the [article online](#) for updates and enhancements.

### You may also like

- [On-chip light detection using integrated microdisk laser and photodetector bonded onto Si board](#)  
Natalia V Kryzhanovskaya, Fedor I Zubov, Eduard I Moiseev et al.
- [Controlling the gain contribution of background emitters in few-quantum-dot microlasers](#)  
F Gericke, M Segnon, M von Helversen et al.
- [Nonlinear emission characteristics of quantum dot–micropillar lasers in the presence of polarized optical feedback](#)  
C Hopfmann, F Albert, C Schneider et al.

# Laser patterning of large-scale perovskite single-crystal-based arrays for single-mode laser displays

Wangqi Mao<sup>1,2</sup>, Haonan Li<sup>2</sup>, Bing Tang<sup>3</sup>, Chi Zhang<sup>4</sup> , Liang Liu<sup>5</sup>, Pei Wang<sup>1</sup>, Hongxing Dong<sup>2,4,\*</sup>  and Long Zhang<sup>1,2,4,\*</sup>

<sup>1</sup> Department of Optics and Optical Engineering, University of Science and Technology of China, Hefei, Anhui 230026, People's Republic of China

<sup>2</sup> Key Laboratory of Materials for High-Power Laser, Shanghai Institute of Optics and Fine Mechanics, Chinese Academy of Sciences, Shanghai 201800, People's Republic of China

<sup>3</sup> Department of Materials Science and Engineering, and Centre for Functional Photonics (CFP), City University of Hong Kong, Hong Kong Special Administrative Region of China 999077, People's Republic of China

<sup>4</sup> School of Physics and Optoelectronic Engineering, Hangzhou Institute for Advanced Study, University of Chinese Academy of Sciences, Hangzhou, Zhejiang 310024, People's Republic of China

<sup>5</sup> Key Laboratory for Micro/Nano Physics and Technology of Hunan Province, State Key Laboratory of Chemo/Biosensing and Chemometrics, College of Materials Science and Engineering, Hunan University, Changsha 410082, People's Republic of China

E-mail: [hongxingd@siom.ac.cn](mailto:hongxingd@siom.ac.cn) and [lzhang@siom.ac.cn](mailto:lzhang@siom.ac.cn)

Received 5 February 2023, revised 9 May 2023

Accepted for publication 21 August 2023

Published 6 September 2023



CrossMark

## Abstract

Lead halide perovskites have attracted considerable attention as potential candidates for high-performance nano/microlasers, owing to their outstanding optical properties. However, the further development of perovskite microlaser arrays (especially based on polycrystalline thin films) produced by the conventional processing techniques is hindered by the chemical instability and surface roughness of the perovskite structures. Herein, we demonstrate a laser patterning of large-scale, highly crystalline perovskite single-crystal films to fabricate reproducible perovskite single-crystal-based microlaser arrays. Perovskite thin films were directly ablated by femtosecond-laser in multiple low-power cycles at a minimum machining line width of approximately 300 nm to realize high-precision, chemically clean, and repeatable fabrication of microdisk arrays. The surface impurities generated during the process can be washed away to avoid external optical loss due to the robustness of the single-crystal film. Moreover, the high-quality, large-sized perovskite single-crystal films can significantly improve the quality of microcavities, thereby realizing a perovskite microdisk laser with narrow linewidth (0.09 nm) and low threshold ( $5.1 \mu\text{J}/\text{cm}^2$ ). Benefiting from the novel laser patterning method and the large-sized perovskite single-crystal films, a high power and high color purity laser display with single-mode microlasers as pixels was successfully fabricated. Thus, this study may offer a potential platform for mass-scale and reproducible fabrication of microlaser arrays, and further facilitate the development of highly integrated applications based on perovskite materials.

\* Authors to whom any correspondence should be addressed.



Original content from this work may be used under the terms of the [Creative Commons Attribution 4.0 licence](https://creativecommons.org/licenses/by/4.0/). Any further distribution of this work must maintain attribution to the author(s) and the title of the work, journal citation and DOI.

Keywords: perovskite single-crystal film, single-mode microlaser, femtosecond-laser processing, laser display

Supplementary material for this article is available [online](#)

## 1. Introduction

Micro/nanolasers with high compactness and emission efficiency have garnered considerable research attention because of their potential applications across several fields, such as on-chip light sources and optical communication. The realization of high-performance micro/nanolasers, particularly laser arrays, requires high-gain materials for compensating optical loss and high-quality resonant cavity arrays for light amplification. Lead halide perovskites are considered one of the most promising candidates for fabricating micro/nanolasers owing to their excellent optical properties [1–7]. Thus far, two types of preparation methods have been developed for perovskite microlasers, namely bottom-up (naturally grown) and top-down methods. In particular, bottom-up perovskite materials have abundant micro/nanostructures that can be used as natural resonators for realizing light amplification. Zhang *et al* synthesized perovskite hemispheres as whispering-gallery-mode (WGM) lasing cavities and achieved high-performance lasing operations with wavelength tunability, emission polarization and thermal stability [8]. Tang *et al* achieved a CsPbBr<sub>3</sub> micro-spherical WGM cavity, from which a low threshold and high laser quality factor were obtained at room temperature [9]. Perovskite microlasers based on these dispersed micro/nanostructures demonstrate unique properties [8–12]. However, the development of single-dispersed micro/nanolasers into controlled laser arrays poses greater practical significance because considerable time and effort have been invested in overcoming the numerous challenges in preparing such materials.

Top-down fabrication is a mature processing technology for mass-scale manufacturing of electronic devices, as it offers high repeatability and controllability advantages [13–15]. Consequently, this technique has been applied to perovskite material systems and excellent lasing performances, including low threshold, unidirectionality, and polarization, have been obtained [16, 17]. However, the high chemical reactivity and inferior thermostability of lead halide perovskite materials prevent their manufacturing using well-established semiconductor fabrication processes [18]. Perovskite microlasers with artificial structures have recently been fabricated using the focused ion beam (FIB) technology [19, 20]. Although FIB involves a high-precision process to control the shape and size of the microcavity, high-intensity ion implantation will damage the intrinsic crystalline quality of perovskite materials, thereby introducing significant optical loss and affecting the performance of microlasers. Alternatively, the femtosecond (fs)-laser processing technology is a new manufacturing tool that provides the advantages of high precision, repeatability, mask-free processing, and a small heat-affected zone [21–23]. Compared to other manufacturing tools, the fs-laser

processing technology accelerates processing efficiency and results in less surface damage and contamination to perovskite materials. However, in the actual experimental process, a series of fundamental and technical problems encountered in fs-laser machining of microcavities structures, such as the uneliminated surface impurities generated during the process and the inadequate machining precision, need further research and exploration. Liang *et al* have proposed effective solutions to these challenges and demonstrated high-precision manufacturing capabilities [24, 25]. Although their solution has certain limitations regarding the preparation of reproducible microcavities that require further technology optimization, we still believe that the fs-laser processing technology may serve as a promising method for the controlled and reproducible fabrication of perovskite microlaser arrays.

The crystallinity of thin films is another essential factor for the top-down fabrication of high-performance microlaser arrays. Most perovskite microlasers reported to date, such as the vertical-cavity laser [26, 27] and distributed feedback laser [28, 29], have been fabricated on only polycrystalline perovskite thin films. Generally, higher trap states are produced by high-density grain boundaries in polycrystalline films, which impacts the charge-carrier lifetimes and causes nonradiative recombination processes that limit the device performance [30, 31]. Consequently, significant efforts have been invested in developing perovskite single-crystal films with high crystalline quality to potentially reduce the optical loss of the resonator and enhance the device's properties [32]. Both solution-based methods [33] (*e.g.* cooling saturated solutions and inverse temperature crystallization) and vapor-phase methods [34] can be used to fabricate perovskite single-crystal films. However, in such solution-based methods, the complicated Cs–Pb–Br phase diagram and the significant solubility difference between CsBr and PbBr<sub>2</sub> in common organic solvents result in the formation of undesired phases during the preparation of single-crystal films, which are detrimental to the optoelectronic properties [35]. Moreover, the residual solvent continually produces defects on the surface of perovskite single crystals. In contrast, the vapor deposition method offers a promising approach to avoid solvent trapping and yield a material with high crystalline quality [36, 37]. Such high-quality perovskite single-crystal films have been successfully employed in photodetectors and solar cells to deliver excellent device performances. However, till date, there is no relevant experimental research on the fabrication of microcavity based on single-crystal films and advanced controllable machining technology. Based on the above analysis, high-quality single-crystal films combined with fs-laser processing technology can achieve higher-quality microcavities that further enhance the lasing performance of pixelated microlaser arrays.

This study prepared a novel solution to precisely fabricate large-scale perovskite single-crystal-based laser arrays using fs-laser processing technology. The chemical vapor deposition (CVD) method was used to prepare large-sized, highly crystalline perovskite single-crystal films on mica substrates. Specifically, the perovskite materials were ablated using an fs-laser in multiple low-power cycles to realize a minimum machining line width of  $\sim 300$  nm, which can pattern the perovskite films into microdisk arrays with high precision. Owing to the perfect single-crystal property, the surface impurities generated during the process can be conveniently washed away by ultrasonic shaking. Stable single-mode lasing from an individual perovskite microlaser was realized at room temperature, and a lasing mode linewidth of 0.09 nm was recorded. Moreover, the size and lasing mode of microlaser arrays can be precisely controlled to overcome the long-standing difficulties of reproducibility and controllability of microlaser arrays. Furthermore, this study demonstrated the possibility of laser display based on perovskite microlaser arrays. Such single-mode microlasers with narrow linewidth serving as a pixel can ensure high power and color purity of the laser display. The compact microlaser arrays produced by these efficient techniques can provide a versatile platform for next-generation integrated photonics.

## 2. Results and discussion

### 2.1. Growth and characterization of single-crystal perovskite films

Large single-crystal  $\text{CsPbX}_3$  films were grown on freshly cleaved mica substrates using an improved vapor method, as shown in figure 1(a). In our experiment, vapor deposition reactant materials were crystallized into microplatelets on the substrate. As the reaction progressed, the platelets increased in size and density, eventually merging into interconnected structures. The thickness of the merged platelets was balanced through lateral growth from the step height difference at the merging boundary, thus yielding a large scale thin film with uniform thickness (figures S1 and S2). A typical optical image of the single-crystal  $\text{CsPbBr}_3$  films is presented in figure 1(b), which depicts well-defined regular shapes and dimensions of up to 1 mm. As reported by previous studies, the formation of the platelet shape is fundamentally governed by the large molecular kinetic energy at high temperatures [38]. Compared to high-pressure environments, a low-pressure environment promotes the production of large-sized seed crystals, as a higher surface-to-volume ratio yields greater seed crystal growth [39]. The detailed analysis of growth dynamics under various temperatures, and pressures are presented in figures S3 and S4. A low-magnification image of the sample observed under scanning electron microscopy (SEM) is portrayed in figure 1(c), which revealed a broad area of the single-crystal  $\text{CsPbBr}_3$  film with no grain boundaries or voids. The local high-magnification SEM image (top-right inset of figure 1(c)) displayed angled facets and smooth surfaces with no grain structures, signifying their single-crystalline features.

In addition, the x-ray diffraction and selected area diffraction characteristics (figure S5) confirmed the appropriate single-crystal properties of the as-prepared films, which corresponded to the orthorhombic phase. Furthermore, the atomic force microscopy images of a single-crystal  $\text{CsPbBr}_3$  film are depicted in figure 1(d), which indicate a high surface smoothness and thickness of 162 nm. Note that this is substantially less than half of the wavelength of the emitted light. However, the optical diffraction limit prevented the formation of the slab microcavity mode, as demonstrated by the absence of the lasing behavior in the fs-laser pumping at room temperature (figure S6). As depicted in figure 1(e), the average surface roughness of a single-crystal  $\text{CsPbBr}_3$  film was measured to be 0.443 nm, which is substantially less than that of the polycrystalline film (16.2 nm) [31]. Thus, such excellent crystalline properties ensure the quality of the laser cavity.

As observed from figure 1(f), the single-crystal  $\text{CsPbBr}_3$  film exhibited optical absorption at wavelengths less than 520 nm (black line, figure 1(f)). Due to film interference, strong oscillations were observed beyond 540 nm, indicating the high smoothness of the single-crystal  $\text{CsPbBr}_3$  film. The photoluminescence (PL) spectrum of the single-crystal  $\text{CsPbBr}_3$  film (red line, figure 1(f)) displayed a peak at 527.5 nm with an ultranarrow full width at half maximum (FWHM:  $\sim 18$  nm, fitted by Lorentz function), indicating the low density of the trap state. The top-right inset of figure 1(f) indicated that the bright and visible green-light emission of the single-crystal  $\text{CsPbBr}_3$  film could be captured using a digital camera, which is consistent with the PL spectrum. To gain a deeper understanding of the optical properties of materials, we measured the PL lifetimes of a single-crystal  $\text{CsPbBr}_3$  film, as shown in the inset of figure 1(f). By fitting the PL lifetimes of the single-crystal  $\text{CsPbBr}_3$  film using a biexponential profile, we obtained values of  $\tau_1 = 7.81$  ns and  $\tau_2 = 22.98$  ns for the two decay components, demonstrating that our single-crystal  $\text{CsPbBr}_3$  film exhibits good crystalline quality and contains fewer surface defects compared to polycrystalline thin films and single-crystalline films prepared using solution-based methods [40]. Therefore, the superior features of the single-crystal  $\text{CsPbBr}_3$  film, including the crystallinity and optical performance, can be beneficial for high-performance micro/nanolasers.

### 2.2. Fabrication of perovskite microdisks

Compared to Fabry–Perot cavities, the WGM cavities generally exhibit ultrahigh  $Q$  factors and small mode volumes owing to their total internal effect [41–43]. In this regard, a disk is an ideal structure for fabricating low-threshold WGM microlasers. As the incident light can be totally reflected, the theoretical cavity  $Q$  factor of a microdisk is considerably higher than that of triangular, square, pentagonal, and hexagonal microcavities [44], as validated by the simulation results (figure S7). Therefore, microdisk cavities were selected for fabricating the microlasers on the single-crystal  $\text{CsPbBr}_3$  film using direct fs-laser ablation.

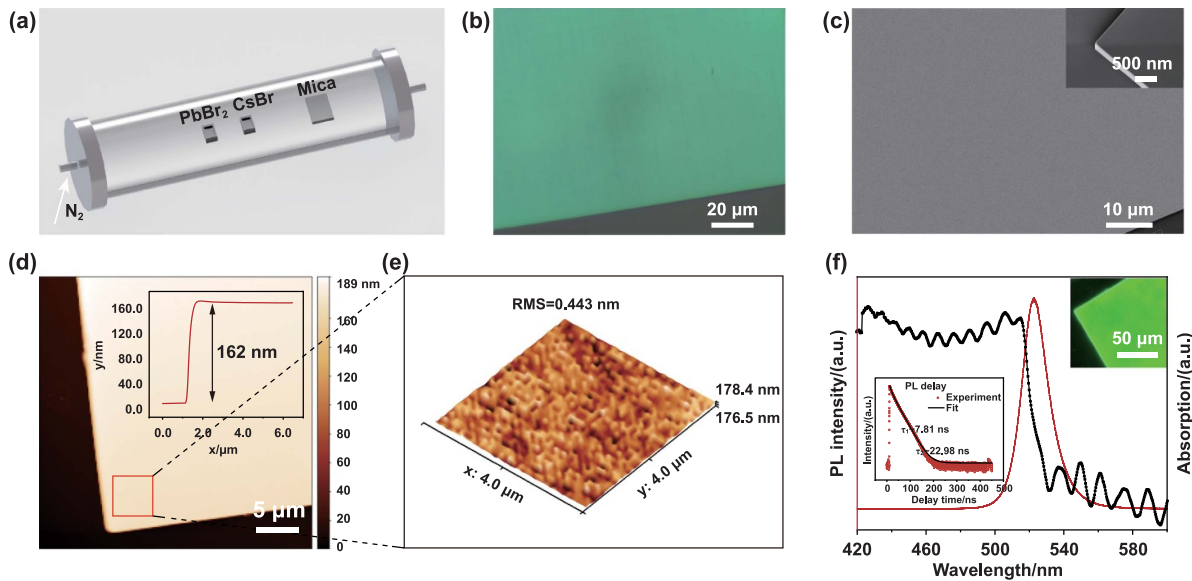


**Figure 1.** Structural and optical characterizations and emission properties of single-crystal CsPbX<sub>3</sub> films. (a) Schematic of CVD method for growing single-crystal CsPbX<sub>3</sub> films on mica substrate. (b) Optical image of CsPbBr<sub>3</sub> films. (c) SEM image of CsPbBr<sub>3</sub> films. [Top inset: the enlarged image of single-crystal CsPbBr<sub>3</sub> film]. (d) AFM image of CsPbBr<sub>3</sub> film; line profile indicates film thickness. (e) AFM image of selected CsPbBr<sub>3</sub> film region with an average surface roughness of 0.443 nm. (f) PL and steady-state absorption spectra of perovskite films [Top inset: fluorescence picture of single-crystal perovskite film. Bottom inset: time-resolved PL decay kinetics of 405 nm photoexcited perovskite single-crystal films].

The schematics of the fabrication of the perovskite microdisks via the fs-laser processing technology are shown in figure 2(a). Laser ablation completely removed the edge of the perovskite microdisks with no visible damage to the remaining microdisks. The SEM images of the microdisks fabricated at a variable number of processing cycles ( $N$ ) and variable fs-laser power ( $P$ ,  $P_{\max} = 260$  mW) are presented in figure 2(b); the images clearly demonstrate the optimization details of the processing parameters. Systematic analysis is shown in figure S10 in supporting information, indicating that the fs-laser power strongly influences microcavity quality. In brief, as the fs-laser power increases, the diameter of microdisks decreases. Moreover, laser-induced thermal effects become more pronounced, and the boundaries become irregular and unsmooth, which can influence the excitation threshold of the perovskite microlasers. Therefore, low-power and multi-cycle laser irradiation were conducted to reduce the damage caused by laser-induced thermal effects. Cleaning and annealing were essential for obtaining cleaner and higher quality microcavities (figure S8). Owing to the high precision and flexibility of the fs-laser processing technology, various sizes of perovskite microdisks can be easily fabricated, as shown in figure 2(c).

In addition, the minimum line width of the processed channel was 300 nm, and the closest distance between the microdisks was approximately 440 nm, thereby rendering it suitable for studying the coupling interaction between microcavities and fabricating novel microlasers with coupling structure (figure S9). The SEM and amplified SEM images of a CsPbBr<sub>3</sub> microdisk array (8 × 8) are shown in figures 2(d) and (e), which demonstrate excellent circular microcavity structure and smooth surface. Evidently, the circular dashed

lines possessed identical dimensions of 6 μm and exhibited near-perfect overlap with each microdisk cavity within the array. Figure 2(f) shows the statistical distribution of microdisk diameters, revealing an average diameter of approximately 6 μm and a minimal margin of error (0.1 μm), inclusive of measurement inaccuracies. This confirms the high precision and repeatability of fs laser processing. Therefore, perfectly shaped, extremely smooth, and size-controlled CsPbBr<sub>3</sub> microdisks are the ideal candidates for fabricating WGM microlasers and studying the internal mechanisms of perovskite microcavity lasers.

### 2.3. Precisely controlled lasing output of WGM microlasers

The laser characteristics of the processed perovskite microdisks were characterized via optical excitation. To ensure a homogeneous excitation, a 400 nm fs-laser was utilized as the excitation light source, wherein the laser spot covered the entire individual microdisk, as illustrated in figure 2(a). The perovskite microdisks displayed a typical characteristic of WGM resonators wherein the laser emission of the perovskite microdisks was the main output of the circular outer boundaries. In particular, the mode spacing between the adjacent laser modes, also known as the free spectral range, is heavily dependent on and inversely proportional to the microdisk radius [45]. Upon reducing the microcavity size, the number of WGM modes in the gain region can be reduced to only one to obtain single-mode lasing.

As depicted in figure 3(a), the number of lasing modes decreases from four to one with the reducing cavity size, thereby resulting in a single-mode lasing output. Finite element method was employed to further analyze the impact of

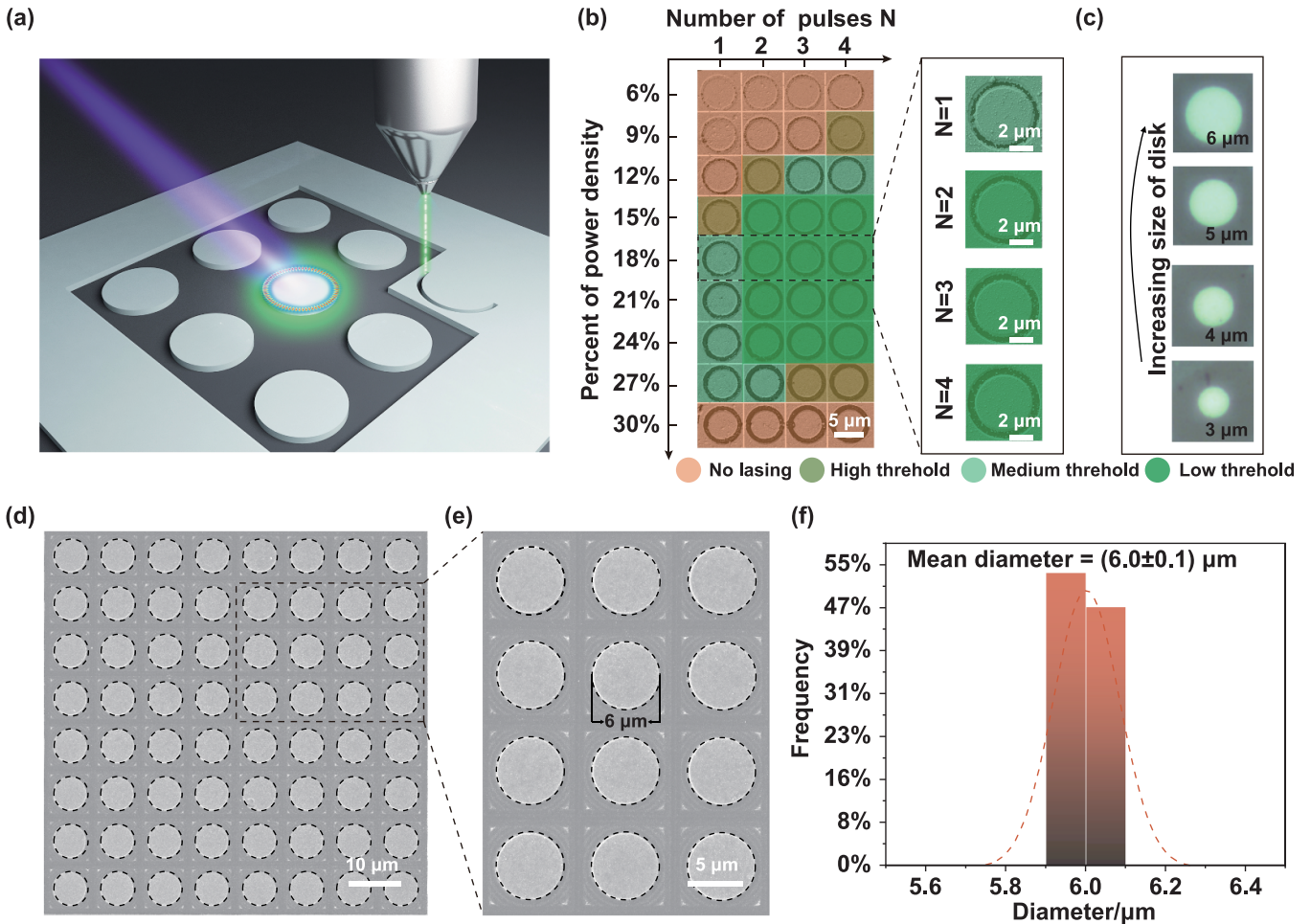


**Figure 2.** Femtosecond-laser-processed perovskite microdisk lasers. (a) Schematics of perovskite microdisks fabrication via fs-laser processing technology. (b) Color-coded SEM image of microdisks fabricated with gradually varying laser power  $P$  (vertical axis:  $P_{\max} = 260$  mW) and number of processing cycles  $N$  (horizontal axis). Magnified image of microdisks fabricated at variable  $N$  and laser power  $P = 18\%$ . Image colors indicated the excitation threshold of perovskite microlasers. (c) Optical images of perovskite microdisks ranging in diameter from  $3 \mu\text{m}$  to  $6 \mu\text{m}$ . (d) SEM image of an  $8 \times 8$  CsPbBr<sub>3</sub> microdisk array. (e) Amplified SEM image of the CsPbBr<sub>3</sub> microdisk array (f) diameter distribution of the CsPbBr<sub>3</sub> microdisk array.

change in cavity size on the resonant mode and  $Q$  factor of the microdisk cavity. The refractive index of the microdisks was set to 2.3, and the diameter of microdisk cavities was set in the range  $2\text{--}8 \mu\text{m}$ . The inset of figure 3(a) shows the simulation results of the electric field distribution with various cavity sizes. Larger diameter microdisks exhibited lower mode spacings with more modes (figure S11), consistent with the experimental results (figure S12). Therefore, the microdisk size can be easily and precisely controlled with the flexibility of the fs-laser processing technology. As was observed, the theoretical cavity  $Q$  factor of the microcavities (figure S13) decreased with decreasing size, thus demonstrating an increased level of cavity loss. The threshold of the pump density with various diameters is shown in figure S14, indicating that the pump energy threshold increases with increase in the disk diameter. A typical pump-density-dependent PL spectrum of a single-mode perovskite microdisk ( $D = 3 \mu\text{m}$ ) is depicted in figure 3(b). A broad PL peak centered at  $527 \text{ nm}$  can be observed if the pump density is below the threshold

of  $5.1 \mu\text{J}/\text{cm}^2$ . As the pump density exceeds this threshold, a single sharp peak emerges at  $538.3 \text{ nm}$ , indicating the occurrence of single-mode lasing. The dependence of the PL peak intensity and FWHM on the pump density is highlighted in figure 3(c). The linearly increasing region of the PL peak intensity below the threshold can be attributed to spontaneous emissions. As the pump density exceeds the threshold, the corresponding outputs increase dramatically because of the stimulated emission and lasing processes [46]. The lasing peaks were fitted by the Lorentz function with a narrow linewidth ( $\delta\lambda$ ) of  $0.09 \text{ nm}$ , as shown in figure 3(d). The Lorentz function was used to address the homogeneous and instrumental broadening to obtain real broadening. The linewidth of this magnitude is competitive for perovskite thin-film single-mode lasers and even comparable to that of naturally grown microcavities (table S1). The prepared perovskite microlasers delivered a high lasing performance and repeatability, thereby rendering them appropriate for use as individual pixels in laser displays.

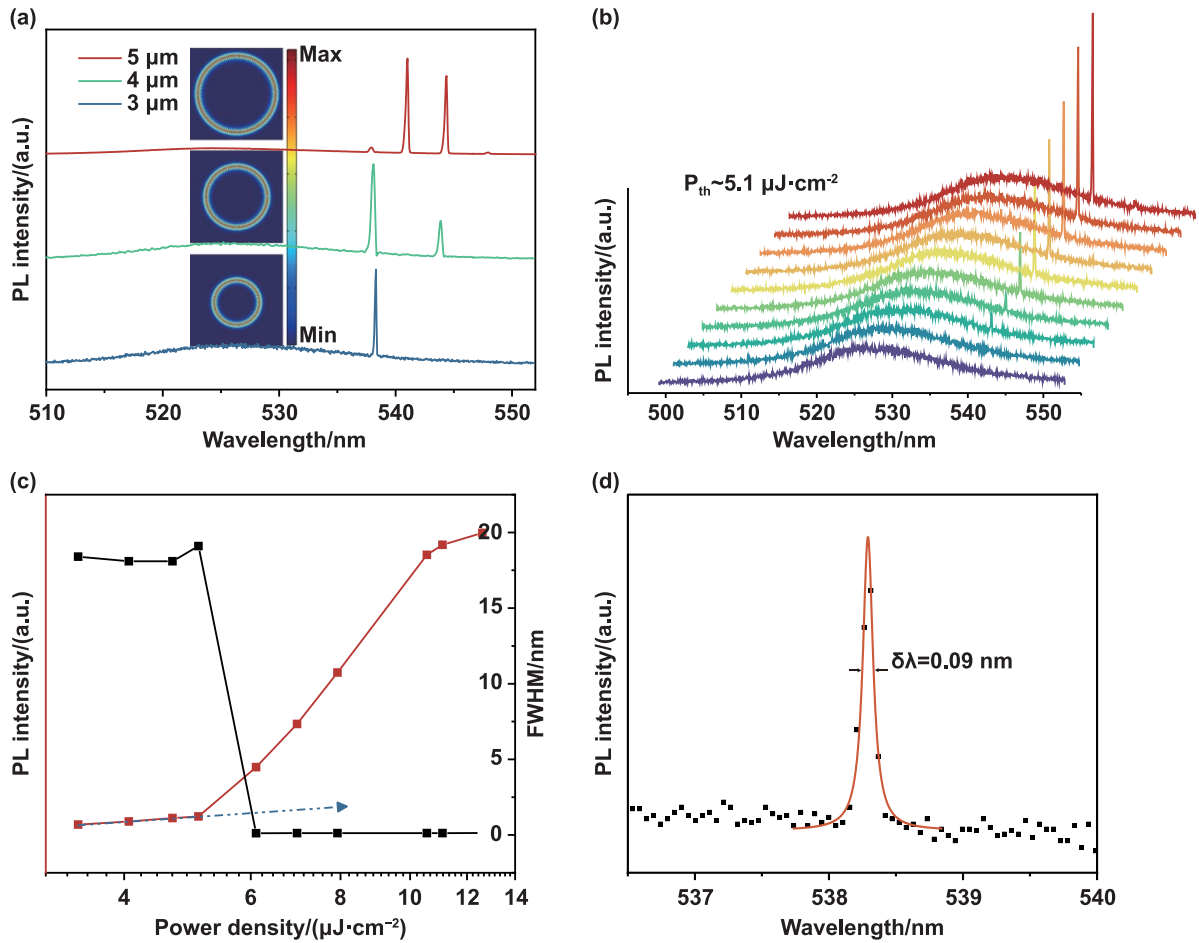


**Figure 3.** Lasing properties of perovskite microdisks. (a) Emission spectrum of perovskite microdisks of diameters varying from 3 μm to 5 μm. (b) Excitation power-dependent lasing spectrum of a single-mode CsPbBr<sub>3</sub> microlaser ( $D = 3 \mu\text{m}$ ). (c) PL intensity and FWHM as a function of pump density. (d) Lorentz fitting of lasing mode, with FWHM of lasing peak ( $\delta\lambda$ ) equal to 0.09 nm.

#### 2.4. Reproducible single-mode microlaser array displays

A perovskite microdisk array composed of equal-sized disks ( $D = 3 \mu\text{m}$ , figure 4(a)) was fabricated to verify whether the fs-laser processing technology could improve the poor repeatability of traditional perovskite microlasers. As observed from figure 4(b), the laser spectra of four disks were captured above the threshold, wherein the lasing modes were almost equal. The results indicate the high repeatability of perovskite microlasers possess because of the high precision of the fs-laser processing technology. Such reproducible perovskite microlasers combined with high lasing performance can be used as laser pixels with various characters (displayed in green in figure 4(c) as the abbreviation ‘CAS’ for the Chinese Academy of Sciences).

As the hybridization states of the Pb and X (halide) orbitals [47] are significant for determining the band gap of halide perovskites (CsPbX<sub>3</sub>), composition engineering may be used to modulate the emission wavelength of the perovskite microdisk laser arrays from 425 nm to 720 nm (figure 4(d)). Among them, microcompositional MA<sup>+</sup>(CH<sub>3</sub>NH<sub>3</sub><sup>+</sup>) was introduced into CsPbI<sub>3</sub> to ensure the stability of the perovskite phase. As observed in figure 4(e), the blue and red microdisk arrays were successfully prepared. In particular, a tunable single-mode

laser with a wavelength range of 475–730 nm can be achieved by adjusting the Cl/Br or Br/I ratios (figure 4(f)). Therefore, patterns with various emission wavelengths (red ‘A,’ green ‘A,’ blue ‘A’) can be facily designed and fabricated, as displayed in the inset of figure 4(f), which demonstrates the high lasing performance of microdisk arrays. A dry transfer method can be employed to transfer the thin-film-based laser array from the top surface of the mica onto other substrates with a modified polypropylene carbonate/poly (methyl methacrylate)-mediated technique [48].

Moreover, the development of high-power, highly stable, and low-threshold electrically pumped perovskite lasers is the ultimate goal in the field. The key attributes for achieving this include highly stable high-quality resonant cavities, and high carrier density [49]. This study proposed a novel approach for constructing efficient perovskite optically pumped lasers through the combination of fs-laser technology with single-crystal thin films, which have immense potential in solving problems for electrically driven laser displays. For electrically pumped perovskite lasers, the high crystalline quality of our microdisk laser can effectively mitigate defect-induced ion migration. Further, high-quality resonant cavities and ultra-thin single-crystal thin films could reduce optical loss and increase current density. When considered all together,

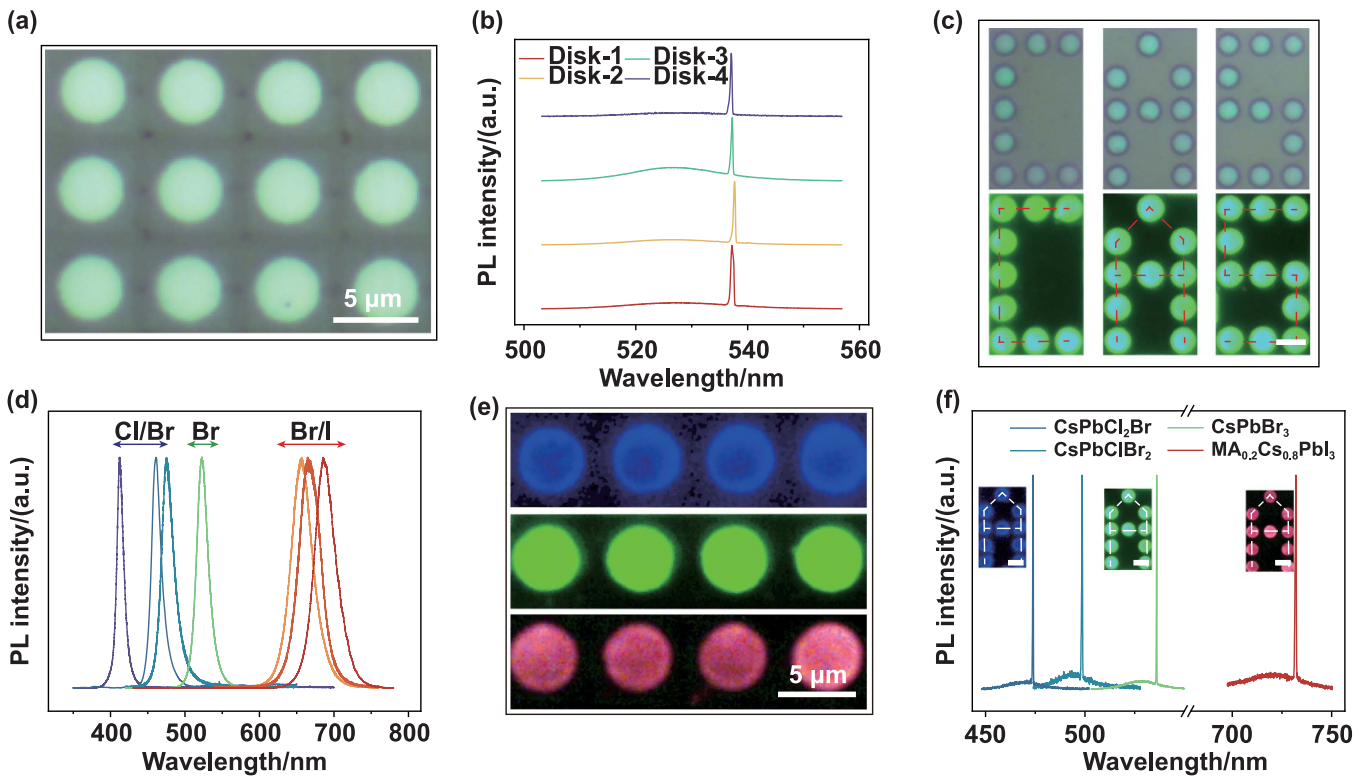


**Figure 4.** Perovskite microlaser arrays for laser displays. (a) Optical image of CsPbBr<sub>3</sub> microlaser array ( $D = 3 \mu\text{m}$ ). (b) Laser spectra of four equal-sized perovskite microdisks. (c) Optical image of CsPbBr<sub>3</sub> microlaser array and far-field photograph of microstructure arrays in 'CAS' patterns of green-color emission. Scale bar:  $5 \mu\text{m}$ . (d) PL spectrum from perovskites with various compositions. (e) Far-field image of MA<sub>0.2</sub>Cs<sub>0.8</sub>PbI<sub>3</sub> (red), CsPbBr<sub>3</sub> (green), and CsPbCl<sub>2</sub>Br (blue). (f) Widely tunable lasing from perovskite microdisk arrays of various compositions. [Top inset: far-field image of microstructure arrays in 'A' patterns of three colors]. Scale bar:  $5 \mu\text{m}$ .

our work has a positive impact on the development of electrically pumped perovskite lasers.

### 3. Conclusions

This study proposed an approach of using single-crystal perovskite films for laser patterning of large-scale single-mode microlaser arrays. Combined with the fs-laser processing technology, large-sized high-quality perovskite single-crystal thin films significantly improved the quality and repeatability of single-mode microlaser arrays. As confirmed by present findings, each processed perovskite microlaser bears a low threshold, narrow linewidth, and repeatability, which enables the utilization of microlasers as individual pixels in laser array displays. Significantly, such extremely compact single-mode microlaser arrays may provide a versatile platform for next-generation integrated photonics.

### 4. Experimental section/methods

#### 4.1. Synthesis of single-crystal CsPbX<sub>3</sub> films

Lead bromide (PbBr<sub>2</sub>, 99.99%), lead iodide (PbI<sub>2</sub>, 99.99%), lead chloride (PbCl<sub>2</sub>, 99.99%), cesium bromide (CsBr, 99.99%), cesium iodide (CsI, 99.99%), cesium chloride (CsCl, 99.99%), methylammonium iodide (MAI, 99.99%) and mica were purchased from Sigma-Aldrich. Large single-crystal

CsPbX<sub>3</sub> films were grown on freshly cleaved mica ([KMg<sub>3</sub>(AlSi<sub>3</sub>)O<sub>10</sub>F<sub>2</sub>]) (001) substrates using an improved vapor method, as shown in figure 1(a). Lead (II) halide was roughly 8 cm away from cesium halide in the upper stream, while 60 sccm of high-purity N<sub>2</sub> gas was introduced into the quartz tube. The evaporated precursors were then moved downstream by flowing argon gas, where a freshly split mica piece was inserted and used as an epitaxial substrate. The furnace was rapidly heated to 630 °C during the growth (600 °C for CsPbI<sub>3</sub>, 630 °C for CsPbBr<sub>3</sub>, 650 °C for CsPbCl<sub>3</sub>). This temperature was maintained for 30 min, and low pressure was maintained inside the tube. Subsequently, the furnace was naturally cooled to room temperature naturally, resulting in the formation of large-sized single-crystal CsPbX<sub>3</sub> films on the mica surface. A field-emission scanning electron microscope (Auriga S40, Zeiss, Oberkochen, Germany) and a scanning near-field optical microscope (neaSNOM, neaspec, Germany) were used to characterize the morphology, structure, and composition of the samples.

#### 4.2. Synthesis of mixed-halide single-crystal CsPb(Cl<sub>x</sub>Br<sub>1-x</sub>)<sub>3</sub> films

To obtain mixed-halide single-crystal CsPbCl<sub>2</sub>Br films, CsBr powder was placed at the center of a CVD furnace, while the equivalent molar mass of PbCl<sub>2</sub> was placed 7 cm away from CsBr in the upper stream. The growth temperature was



set to 630 °C, and the other procedures were the same as presented above. After approximately 30 min, single-crystal CsPbCl<sub>2</sub>Br films were obtained successfully. To obtain single-crystal CsPbClBr<sub>2</sub> films, CsCl powder was placed at the center of a CVD furnace, while the equivalent molar mass of PbBr<sub>2</sub> was placed 8 cm away from CsCl in the upper stream. The growth temperature was set to 650 °C, and the other procedures were the same as above. After approximately 30 min, single-crystal CsPbClBr<sub>2</sub> films were obtained successfully.

#### 4.3. Synthesis of MA<sub>0.2</sub>Cs<sub>0.8</sub>PbI<sub>3</sub> perovskite films

The MAI powder was placed at the center of a CVD furnace, while the substrates with CsPbI<sub>3</sub> perovskite microlasers were placed above the MAI. During the whole vapor conversion process, the temperature was 157 °C, and pressure was atmospheric pressure with a controlled N<sub>2</sub> gas flow rate of 120 sccm. After approximately 20 min, MA<sub>0.2</sub>Cs<sub>0.8</sub>PbI<sub>3</sub> perovskite films were prepared successfully.

#### 4.4. Fabrication of perovskite microlasers by fs-laser

Perovskite microdisk lasers were fabricated using a 520 nm-fs-laser with 100 kHz laser pulses from a Ti:sapphire laser system. The fs-laser power was set at 18% of  $P$  ( $P_{\max} = 260$  mW). The fs-laser was focused using a dry microscope objective (100, numerical aperture = 0.9, working distance = 1 mm), resulting in a spot diameter of about 300 nm. The perovskite films were placed on a PC-driven nanopositioning system with an accuracy of more than 100 nm along all three axes. The marking speed, pulse density, and burst mode (figure S15) were set at 0.02 mm s<sup>-1</sup>, 30 000 pulses mm<sup>-1</sup>, and 100 respectively. The fabricated perovskite microlasers were immersed in toluene and ultrasonically cleaned for 1 min to remove the debris generated during the process. Next, the samples were placed in an annealing furnace and annealed for 10 min at 200 °C under N<sub>2</sub>.

#### 4.5. Optical measurement and simulation details

PL and lasing emissions were measured at room temperature using a laser confocal microphotoluminescence system (LabRAM HR Evolution) and a 400 nm fs-pulsed laser (~40 fs, 10 kHz). A 400 nm fs-laser (repetition rate of 1 kHz, pulse width of 80 fs) equipped with a streak camera (C10910, Hamamatsu) was used to perform time-resolved PL measurements. The lasing mode properties, including the electric-field distributions,  $Q$  factor, and far-field azimuthal distribution, were calculated using the finite element method.

### Acknowledgments

The authors acknowledge the support from the National Natural Science Foundation of China (No. 61925506), the Natural Science Foundation of Shanghai (No. 20JC1414605) and Hangzhou Science and Technology Bureau of Zhejiang Province (No. TD2020002). H D acknowledges the

Academic/Technology Research Leader Program of Shanghai (23XD1404500).

### ORCID iDs

Chi Zhang  <https://orcid.org/0000-0003-3823-7794>

Hongxing Dong  <https://orcid.org/0000-0001-9584-9899>

### References

- [1] Hu Z, Liu Z Z, Zhan Z, Shi T C, Du J, Tang X S and Leng Y X 2021 Advances in metal halide perovskite lasers: synthetic strategies, morphology control, and lasing emission *Adv. Photon.* **3** 034002
- [2] Sutherland B R and Sargent E H 2016 Perovskite photonic sources *Nat. Photon.* **10** 295–302
- [3] Wang K Y, Wang S, Xiao S M and Song Q H 2018 Recent advances in perovskite micro- and nanolasers *Adv. Opt. Mater.* **6** 1800278
- [4] Zhang Q, Diederichs C and Xiong Q H 2020 Golden hour for perovskite photonics *Photonics Res.* **8** 1–PP4
- [5] Zhang Q, Su R, Du W N, Liu X F, Zhao L Y, Ha S T and Xiong Q H 2017 Advances in small perovskite-based lasers *Small Methods* **1** 1700163
- [6] Li Z T, Cao K, Li J S, Tang Y, Ding X R and Yu B H 2021 Review of blue perovskite light emitting diodes with optimization strategies for perovskite film and device structure *Opto-Electron. Adv.* **4** 200019
- [7] Yan D D, Zhao S Y, Zhang Y B, Wang H X and Zang Z G 2022 Highly efficient emission and high-CRI warm white light-emitting diodes from ligand-modified CsPbBr<sub>3</sub> quantum dots *Opto-Electron. Adv.* **5** 200075
- [8] Zhang H B et al 2020 Lasing operation in the CsPbBr<sub>3</sub> perovskite micron hemisphere cavity grown by chemical vapor deposition *Chem. Eng. J.* **389** 124395
- [9] Tang B, Dong H X, Sun L X, Zheng W H, Wang Q, Sun F F, Jiang X W, Pan A L and Zhang L 2017 Single-mode lasers based on cesium lead halide perovskite submicron spheres *ACS Nano* **11** 10681–8
- [10] Feng L, Wong Z J, Ma R M, Wang Y and Zhang X 2014 Single-mode laser by parity-time symmetry breaking *Science* **346** 972–5
- [11] Li Y J, Lv Y C, Zou C L, Zhang W, Yao J N and Zhao Y S 2016 Output coupling of perovskite lasers from embedded nanoscale plasmonic waveguides *J. Am. Chem. Soc.* **138** 2122–5
- [12] Zhu H M, Fu Y P, Meng F, Wu X X, Gong Z Z, Ding Q, Gustafsson M V, Trinh M T, Jin S and Zhu X Y 2015 Lead halide perovskite nanowire lasers with low lasing thresholds and high quality factors *Nat. Mater.* **14** 636–42
- [13] Geng D C, Wang H P, Wan Y, Xu Z P, Luo B R, Xu J and Yu G 2015 Direct top-down fabrication of large-area graphene arrays by an in situ etching method *Adv. Mater.* **27** 4195–9
- [14] Naureen S, Shahid N, Sanatinia R and Anand S 2013 Top-down fabrication of high quality III–V nanostructures by monolayer controlled sculpting and simultaneous passivation *Adv. Funct. Mater.* **23** 1620–7
- [15] Chen Y Q, Shu Z W, Zhang S, Zeng P, Liang H K, Zheng M J and Duan H G 2021 Sub-10 nm fabrication: methods and applications *Int. J. Extrem. Manuf.* **3** 032002
- [16] Cegielski P J et al 2018 Monolithically integrated perovskite semiconductor lasers on silicon photonic chips by scalable top-down fabrication *Nano Lett.* **18** 6915–23
- [17] Bar-On O, Brenner P, Lemmer U and Scheuer J 2018 Micro lasers by scalable lithography of metal-halide perovskites *Adv. Mater. Technol.* **3** 1800212

- [18] Manser J S, Saidaminov M I, Christians J A, Bakr O M and Kamat P V 2016 Making and breaking of lead halide perovskites *Acc. Chem. Res.* **49** 330–8
- [19] Alias M S, Yang Y, Ng T K, Dursun I, Shi D, Saidaminov M I, Priante D, Bakr O M and Ooi B S 2016 Enhanced etching, surface damage recovery, and submicron patterning of hybrid perovskites using a chemically gas-assisted focused-ion beam for subwavelength grating photonic applications *J. Phys. Chem. Lett.* **7** 137–42
- [20] Alias M S, Dursun I, Shi D, Saidaminov M I, Diallo E M, Priante D, Ng T K, Bakr O M and Ooi B S 2015 Focused-ion beam patterning of organolead trihalide perovskite for subwavelength grating nanophotonic applications *J. Vac. Sci. Technol. B* **33** 051207
- [21] Zhizhchenko A et al 2019 Single-mode lasing from imprinted halide-perovskite microdisks *ACS Nano* **13** 4140–7
- [22] Liang L M, Ma T, Chen Z Y, Wang J X, Hu J N, Ji Y C, Shen W L and Chen J 2023 Patterning technologies for metal halide perovskites: a review *Adv. Mater. Technol.* **8** 2200419
- [23] Guo Y, Qiu P, Xu S L and Cheng G J 2022 Laser-induced microjet-assisted ablation for high-quality microfabrication *Int. J. Extrem. Manuf.* **4** 035101
- [24] Liang S Y, Liu Y F, Hua J G, Ji Z K and Xia H 2023 Femtosecond laser regulatory focus ablation patterning of a fluorescent film up to 1/10 of the scale of the diffraction limit *Nanoscale* **15** 5494–8
- [25] Liang S Y, Liu Y F, Zhang H J, Ji Z K and Xia H 2022 High-quality patterning of CsPbBr<sub>3</sub> perovskite films through lamination-assisted femtosecond laser ablation toward light-emitting diodes *ACS Appl. Mater. Interfaces* **14** 46958–63
- [26] Sun W Z, Liu Y L, Qu G Y, Fan Y B, Dai W, Wang Y H, Song Q H, Han J C and Xiao S M 2020 Lead halide perovskite vortex microlasers *Nat. Commun.* **11** 4862
- [27] Wang Y, Li X M, Nalla V, Zeng H B and Sun H D 2017 Solution-processed low threshold vertical cavity surface emitting lasers from all-inorganic perovskite nanocrystals *Adv. Funct. Mater.* **27** 1605088
- [28] Allegro I, Bonal V, Mamleyev E R, Villalvilla J M, Quintana J A, Jin Q H, Díaz-García M A and Lemmer U 2023 Distributed feedback lasers by thermal nanoimprint of perovskites using gelatin gratings *ACS Appl. Mater. Interfaces* **15** 8436–45
- [29] Dong Q et al 2022 Cavity engineering of perovskite distributed feedback lasers *ACS Photonics* **9** 3124–33
- [30] Zhang W et al 2015 Ultrasoft organic-inorganic perovskite thin-film formation and crystallization for efficient planar heterojunction solar cells *Nat. Commun.* **6** 6142
- [31] Doherty T A S et al 2020 Performance-limiting nanoscale trap clusters at grain junctions in halide perovskites *Nature* **580** 360–6
- [32] Dong Q F, Fang Y J, Shao Y C, Mulligan P, Qiu J, Cao L and Huang J S 2015 Electron-hole diffusion lengths >175 μm in solution-grown CH<sub>3</sub>NH<sub>3</sub>PbI<sub>3</sub> single crystals *Science* **347** 967–70
- [33] Li L Y, Liu J X, Zeng M Q and Fu L 2021 Space-confined growth of metal halide perovskite crystal films *Nano Res.* **14** 1609–24
- [34] Dunlap-Shohl W A, Zhou Y Y, Padture N P and Mitzi D B 2019 Synthetic approaches for halide perovskite thin films *Chem. Rev.* **119** 3193–295
- [35] Zhang H J, Liu X, Dong J P, Yu H, Zhou C, Zhang B B, Xu Y D and Jie W Q 2017 Centimeter-sized inorganic lead halide perovskite CsPbBr<sub>3</sub> crystals grown by an improved solution method *Cryst. Growth Des.* **17** 6426–31
- [36] Jiang J et al 2019 Carrier lifetime enhancement in halide perovskite via remote epitaxy *Nat. Commun.* **10** 4145
- [37] Zhou Y et al 2021 Millimeter-size all-inorganic perovskite crystalline thin film grown by chemical vapor deposition *Adv. Funct. Mater.* **31** 2101058
- [38] Shoaib M et al 2017 Directional growth of ultralong CsPbBr<sub>3</sub> perovskite nanowires for high-performance photodetectors *J. Am. Chem. Soc.* **139** 15592–5
- [39] Li C, Zhao L Y, Fan H, Shang Q Y, Du W N, Shi J W, Zhao Y, Liu X F and Zhang Q 2020 Graphoepitaxy of large scale, highly ordered CsPbBr<sub>3</sub> nanowire array on muscovite mica (001) driven by surface reconstructed grooves *Adv. Opt. Mater.* **8** 2000743
- [40] Liu G D, Jia S T, Wang J, Li Y F, Yang H, Wang S F and Gong Q H 2021 Toward microlasers with artificial structure based on single-crystal ultrathin perovskite films *Nano Lett.* **21** 8650–6
- [41] Yang Y D, Tang M, Wang F L, Xiao Z X, Xiao J L and Huang Y Z 2019 Whispering-gallery mode hexagonal micro-/nanocavity lasers [Invited] *Photon. Res.* **7** 594–607
- [42] Liu W, Li Z X, Shi Z L, Wang R, Zhu Y Z and Xu C X 2021 Nano-buffer controlled electron tunneling to regulate heterojunctional interface emission *Opto-Electron. Adv.* **4** 200064
- [43] Zheng Y, Wu Z F, Shum P P, Xu Z L, Keiser G, Humbert G, Zhang H L, Zeng S W and Dinh X Q 2018 Sensing and lasing applications of whispering gallery mode microresonators *Opto-Electron. Adv.* **1** 180015
- [44] Wang K, Liang J, Chen R, Gao Z H, Zhang C, Yan Y L, Yao J N and Zhao Y S 2021 Geometry-programmable perovskite microlaser patterns for two-dimensional optical encryption *Nano Lett.* **21** 6792–9
- [45] Lu J F et al 2019 Dynamic regulating of single-mode lasing in ZnO microcavity by piezoelectric effect *Mater. Today* **24** 33–40
- [46] Samuel I D W, Namdas E B and Turnbull G A 2009 How to recognize lasing *Nat. Photon.* **3** 546–9
- [47] Fu Y P, Zhu H M, Stoumpos C C, Ding Q, Wang J, Kanatzidis M G, Zhu X Y and Jin S 2016 Broad wavelength tunable robust lasing from single-crystal nanowires of cesium lead halide perovskites (CsPbX<sub>3</sub>, X = Cl, Br, I) *ACS Nano* **10** 7963–72
- [48] Wang R Y, Muhammad Y, Xu X, Ran M, Zhang Q F, Zhong J C, Zhuge F W, Li H Q, Gan L and Zhai T Y 2020 Facilitating all-inorganic halide perovskites fabrication in confined-space deposition *Small Methods* **4** 2000102
- [49] Liu A Q, Guan G Y, Chai X M, Feng N N, Lu M, Bai X and Zhang Y 2022 Metal halide perovskites toward electrically pumped lasers *Laser Photon. Rev.* **16** 2200189